Modeling and Analysis of MHz-Frequency PRC-$LCLC$ Resonant Converter Utilizing Only Parasitic Capacitance From Planar Transformer and Cockcroft–Walton Voltage Multiplier as Parallel Capacitor

Runze Wang, Saijun Mao, *Senior Member, IEEE*, Shan Yin, *Member, IEEE*, Jinshu Lin, *Student Member, IEEE*, Hongyao Liu, Hui Li, *Senior Member, IEEE*, and Jiajie Fan, *Senior Member, IEEE*

***Abstract*—High-frequency planar transformers and Cockcroft–Walton (CW) rectifiers are essential for developing miniaturized and high-power-density high voltage generators. Parallel resonant converters (PRCs) are commonly used for parasitics integration and high-efficiency operation. However, modeling and designing PRC-$LCLC$ resonant converters with planar transformers and CW voltage multipliers are challenging due to the significant nonlinear parasitics from rectifier diodes and the compensation effects in the resonant tank caused by the discontinuity of rectifier current. To address these challenges, this work proposes a model incorporating nonlinear parasitic capacitance based on the rectified-compensation fundamental mode approximation (RCFMA) method. A novel normalized analysis is conducted on the basis of the resonant frequency of the parallel branch of the RCFMA model, which separates the series-branch-based PRC-$LCLC$ resonant characteristics from the compensation effect of rectifier and nonlinear parasitic capacitance. Furthermore, a voltage-oriented design methodology is introduced. The methodology utilizes the components of the series branch to achieve the step-up voltage gain and zero voltage switching condition for the PRC-$LCLC$ resonant tank. Simultaneously, the parallel branch effectively manages compensation effects and nonlinear parasitic parameters without external capacitors. The proposed design methodology enhances the high-frequency design feasibility, improves the parasitics integration and resolves the conflict between the characteristics design, compensation effects, and the nonlinear parasitic parameters utilization compared to traditional analysis-based designs of PRC-$LCLC$ resonant converters. Finally, the RCFMA model and design methodology are verified through experiments with a gallium nitride-based 25-V/1000-V MHz-frequency PRC-$LCLC$ resonant converter.**

***Index Terms*—Cockcroft–Walton (CW) voltage multiplier, gallium nitride (GaN), high frequency, high step-up converter, high-voltage generator, parallel resonant converter (PRC), planar transformer, PRC-$LCLC$ resonant converter, rectified-compensation fundamental mode approximation (RCFMA).**

I. Introduction

THE trend toward miniaturization and lightweight design of the high-voltage generator is critically essential for portable X-ray machines [1], [2], electrostatic precipitators (ESPs) [3], magnetrons [4], and particularly for the electric propulsion (EP) systems of satellites [5], [6], [7]. To achieve extremely high voltage gain and miniaturized design simultaneously, step-up parallel resonant converters (PRCs) are a common choice. These converters effectively integrate parasitics, achieve zero voltage switching (ZVS), and reduce electromagnetic interference (EMI) [8].

The typical block diagram of a resonant step-up converter is illustrated in Fig. 1, where the step-up ratio can be achieved not only by the transformer, but also by the rectifier as well as the resonant tank. To mitigate the nonidealities induced by the extremely high turn-ratio transformer, the Cockcroft–Walton (CW) voltage multiplier is popular due to its high voltage gain, simple topology, and low voltage stress [4], [9], [10]. In addition, the planar transformer has emerged as an enabling technology characterized by low profiles, easy manufacturing, and reproducible parameters compared to traditional bulky transformers [11], [12], [13]. This combination of transformer and rectifier offers reduced size and enhanced performance, making it attractive for compact and high-power-density step-up converters [5], [6], [14].

Received 29 July 2024; revised 13 October 2024 and 1 December 2024; accepted 13 December 2024. Date of publication 17 December 2024; date of current version 28 January 2025. This work was supported by National Natural Science Foundation of China under Grant 52275559. Recommended for publication by Associate Editor M. Ferdowsi. *(Corresponding author: Jiajie Fan.)*

Runze Wang and Jiajie Fan are with the Institute of Future Lighting, Academy for Engineering and Technology, Shanghai Engineering Technology Research Center of SiC Power Device, Fudan University, Shanghai 200433, China, also with the Research Institute, Fudan University in Ningbo, Ningbo 315336, China (e-mail: rzwang21@m.fudan.edu.cn; jiajie_fan@fudan.edu.cn).

Saijun Mao and Hongyao Liu are with the UniSic Technology Shanghai Company Ltd., Shanghai 201210, China (e-mail: saijun.mao@unisic.tech; hongyao.liu@unisic.tech).

Shan Yin is with the Huawei Technologies Company Ltd., Shenzhen 518129, China (e-mail: yinshan4@huawei.com).

Jinshu Lin and Hui Li are with the School of Aeronautics and Astronautics, University of Electronic Science and Technology of China, Chengdu 611731, China (e-mail: linjinshu@std.uestc.edu.cn; kelly.li@uestc.edu.cn).

Color versions of one or more figures in this article are available at https://doi.org/10.1109/TPEL.2024.3519356.

Digital Object Identifier 10.1109/TPEL.2024.3519356

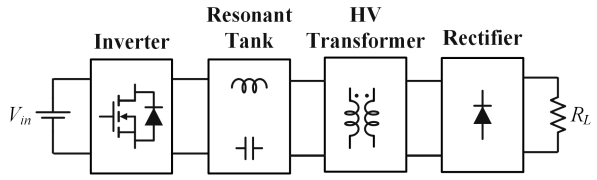

Fig. 1. Block diagram of resonant step-up converter.

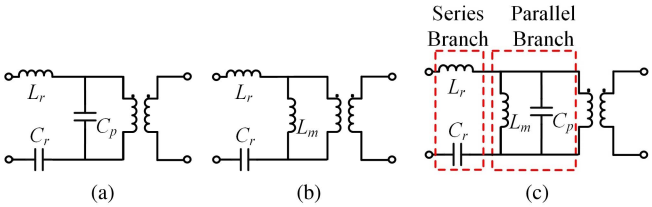

Fig. 2. Comparison of different resonant tanks. (a) PRC-LCC. (b) LLC. (c) PRC-$LCLC$.

One of the challenges faced by the most popular resonant converters is that both the PRC-LCC and LLC resonant converters shown in Fig. 2(a) and 2(b) cannot fully integrate the parasitics induced by the aforementioned transformer–rectifier (T–R) set. Specifically, due to the limitation of the window area of the step-up planar transformer, the number of primary turns is constrained and the magnetic inductance L_m ranges from several to tens of μH [11], [14], which cannot satisfy the assumption of the large enough L_m for the PRC-LCC resonant converter. Simultaneously, the parasitic capacitance originating from the secondary winding C_w of the transformer and the junction capacitance C_j of the rectifier diodes will be amplified by n^2 when they are reflected to the primary side of the transformer, where 1:n is the turn ratio of the step-up transformer. In addition, although silicon carbide (SiC) diodes have excellent performance at high operation frequencies, spanning several hundreds of kHz to MHz, the junction capacitance C_j of SiC diodes is several times larger than that of silicon (Si) diodes under the same voltage rating [15]. In this case, the parasitic capacitance increases to several tens of nF, whereas the LLC resonant converter can only tackle the parasitic capacitance of tens of pF [16], [17], [18]. For comparison, the PRC-$LCLC$ resonant converter, as depicted in Fig. 2(c), combines the PRC-LCC and LLC resonant converter and enables the incorporation of L_m, C_w, and C_j, which is a promising topology for the miniaturized converter with a high step-up ratio [14], [19], [20], [21].

The modeling and analysis of the PRC-$LCLC$ resonant converter fed by the CW voltage multiplier is still a challenge to be solved. Time-domain based modeling methods are proved to be cumbersome due to the multiple resonant components, complex operating modes, and nonliearities effects from T–R set [1], [2], [22]. The traditional fundamental mode approximation (FMA), as a relatively simpler and intuitive method, is moderately accurate for the resonant converter with the LC filter [23], [24]. However, the rectifier with the capacitive filter brings considerable errors for the voltage-fed PRC resonant converters, where the current flowing into the rectifier becomes discontinuous [25]. To solve this problem, a rectifier-compensated FMA (RCFMA) analysis introduces an RC network with the improved accuracy. These linearized models provide a detailed description of the resonant converters with the full-bridge rectifier [3], [14], [19], [20], [26], [27]. Unfortunately, most state-of-the-art steady-state models of the resonant converter with the CW voltage multiplier rectifier are deduced only for the PRC-LCC resonant converter [2].

The next challenge in designing the PRC-$LCLC$ resonant converter is addressing the nonlinear parasitics from rectifier diodes and compensation effects associated with rectifier behavior. Typically, setting f_s at the resonant frequency of the series branch of PRCs f_{ser} is widely adopted in high-voltage generator applications [5], [19], [20], [28]. In this case, the characteristics of the PRC-$LCLC$ resonant converter can be further deduced based on the normalized analysis of f_{ser}, which is the function of the capacitor ratio $C_n = C_r/C_p$ and the inductor ratio $L_n = L_m/L_r$. Based on these conditions, the resonant components of the parallel branch can be determined by the predetermined L_n and C_n. However, significant limitations arise with this design method for PRC-$LCLC$ resonant converters with the high-gain voltage-multiplier rectifier circuits. These challenges include: 1) Limited design freedom of resonant tank gain: The voltage gain of the resonant tank is constrained around unity, significantly reducing the flexibility in designing the voltage gain of the resonant tank [7], [14], [19], [29]. 2) The necessity of adjusting the parallel branch: The parallel branch elements are required to adjust the impedance of the PRC-$LCLC$ resonant tank. a) Adjustable L_m: Modifying L_m is often necessary to achieve the desired resonant frequency of the parallel branch f_{par}, which is both time-consuming and costly [5], [29]. b) External C_p: While the parasitic capacitance (C_j, C_w) and the equivalent capacitance due to the rectifier compensation effect are considerable, adding an external parallel capacitor is a common approach to adjusting the impedance of the resonant tank in various PRC design methodologies [4], [7], [14], [30]. 3) The feasibility of high f_s and pulse frequency modulation (PFM): The high-frequency operation of the PRC-$LCLC$ resonant converter under power transmission conditions is generally avoided due to the significant impact of the parallel branch [14], [19]. Although some studies have attempted to improve f_s to the MHz range by raising f_{par}, the wide-load regulation under ZVS condition through the simple PFM remains unsupported due to the constraints imposed by the parallel branch [5], [29]. The comparison of the design methodologies of PRC-$LCLC$ resonant converter is summarized in Table I.

In this work, a RCFMA model considering parasitics is established for the PRC-$LCLC$ resonant converter with the planar transformer and the CW voltage multiplier. The normalized analysis of the RCFMA model is conducted according to the resonant frequency of the parallel branch. Leveraging the established model and the normalized analysis, a voltage-oriented design methodology is proposed for the PRC-$LCLC$ resonant converter with the specified T–R set. The design approach takes full utilization of the characteristics of the PRC-$LCLC$ resonant tank. The two parameters L_m and C_p are flexible to

TABLE I
DESIGN METHODOLOGICAL COMPARISON OF PRC-$LCLC$ RESONANT CONVERTER

Ref. and time	Rectifier type	Voltage gain of T-R set	Voltage gain design of resonant tank	Adjusting parallel branch		High f_s implementation	PFM implementation
				Adjustable L_m	External C_p		
[19] 2011	Full bridge	43	Unsupported	Not required	Not required	Unsupported, 100 kHz	Unsupported
[14] 2017	Voltage doubler	120	Unsupported	Not required	Required, 15 nF	Unsupported, 500 kHz	Unsupported
[5] 2022	CW Voltage multiplier	92	Unsupported	Required	Not required	Supported, 1.2 MHz	Unsupported
[29] 2025	Dickson voltage multiplier	45	Unsupported	Required	Not required	Supported, 1.7 MHz	Unsupported
This work	CW voltage multiplier	80	Supported	Not required	Not required	Supported, 0.9 $\sim$ 1.5 MHz	Supported

accommodate the parameters induced by the planar transformer and CW voltage multiplier set. After that, the functions of desired voltage gain and ZVS condition for the PRC-$LCLC$ resonant tank are achieved by adjusting L_r and C_r. Finally, the RCFMA model and comprehensive design only utilizing the parasitic capacitance as C_p are given and verified through a 25-V input, 1-kV output, MHz-frequency PRC-$LCLC$ resonant converter prototype with the planar transformer and CW voltage multiplier.

The rest of this article is organized as follows. Section II introduces the steady-state model of the PRC-$LCLC$ resonant converter, taking the parasitics induced by the planar transformer and CW voltage multiplier into account. Besides, the voltage gain, the impedance of the resonant tank and the component stress of the PRC-$LCLC$ resonant converter are derived based on the normalized analysis of the parallel branch of the RCFMA model. Section III provides a detailed voltage-oriented design methodology for the PRC-$LCLC$ resonant converter. Section IV validates the derived RCFMA model and the design methodology with the experimental testing results of the PRC-$LCLC$ resonant converter hardware prototype. Section V provides discussion. Finally, Section VI concludes this article.

The main contributions of this article are as follows.

1) A RCFMA model is proposed for the PRC-$LCLC$ resonant converter with the planar transformer and CW voltage multiplier. This model accounts for the nonlinear parasitic capacitance, the compensation effect of the rectifier behavior, and the conversion efficiency.
2) A novel normalized analysis of the RCFMA model is presented to address the conflicts between the resonant tank characteristics design and nonlinear parasitic capacitance as well as the rectifier-behavior compensation effect.
3) A voltage-oriented method is proposed, which can improve parasitic capacitance integration and enhance the high-frequency implementation feasibility by decoupling the series branch-based PRC-$LCLC$ resonant characteristics from the compensation effect of rectifier behavior and the nonlinear effect of parasitic capacitance.
4) A 25-V input, 1-kV output, MHz-frequency PRC-$LCLC$ resonant converter prototype is built. In this prototype, the parallel capacitor is comprised solely of the parasitic capacitance of the T–R set.

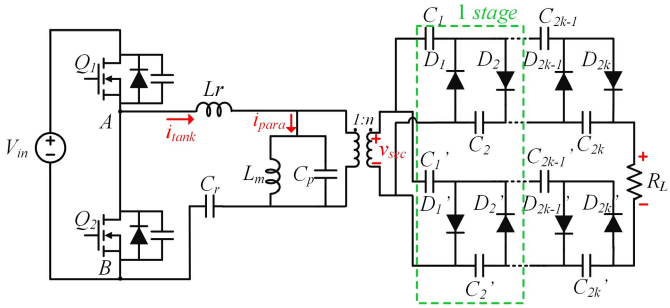

Fig. 3. Circuit diagram of PRC-$LCLC$ resonant converter.

II. STEADY-STATE CIRCUIT MODELING AND ANALYSIS OF THE STEP-UP CONVERTER

A. Operation Modes Analysis and C_j Estimation

The circuit diagram of the PRC-$LCLC$ resonant converter with the dual-polarity CW voltage multiplier is shown in Fig. 3, where L_r is the resonant inductor, C_p includes the winding parasitic capacitance C_w and the diode junction capacitance C_j, k is the stage number for the dual-polarity CW voltage multiplier, n is the turn ratio of the transformer, and R_L is the load resistance.

The operation condition of the PRC-$LCLC$ resonant converter can divided into two main modes during the half switching period:

1) Mode 1($t_0 \sim t_1$): During this mode, the parallel branch is not clamped, and both L_m and C_p join into the resonance. The current of resonant tank i_{tank} continues to decrease until it crosses zero. After that, i_{tank} increases reversely. In addition, C_j of D_{2k-1} and D'_{2k} (D_{2k} and D'_{2k-1}) are discharged (charged) during this mode. This mode ends at t_1 when the rectifier starts to conduct and the parallel branch will be reclamped by the output voltage. The conduction state of the PRC-$LCLC$ resonant converter is shown in Fig. 4(a).

2) Mode 2 ($t_1 \sim t_2$): This mode starts when the voltage of the parallel branch of the PRC-$LCLC$ resonant tank is clamped by the output voltage. The odd diodes D_{2k-1} and even diodes D'_{2k} start conducting for the up-side and down-side CW voltage multipliers, respectively. During this mode, L_m and C_p do not participate in the resonance, and the PRC-$LCLC$ resonant converter works like a series resonant converter as shown in Fig. 4(b). This mode ends when all the diodes are blocked.

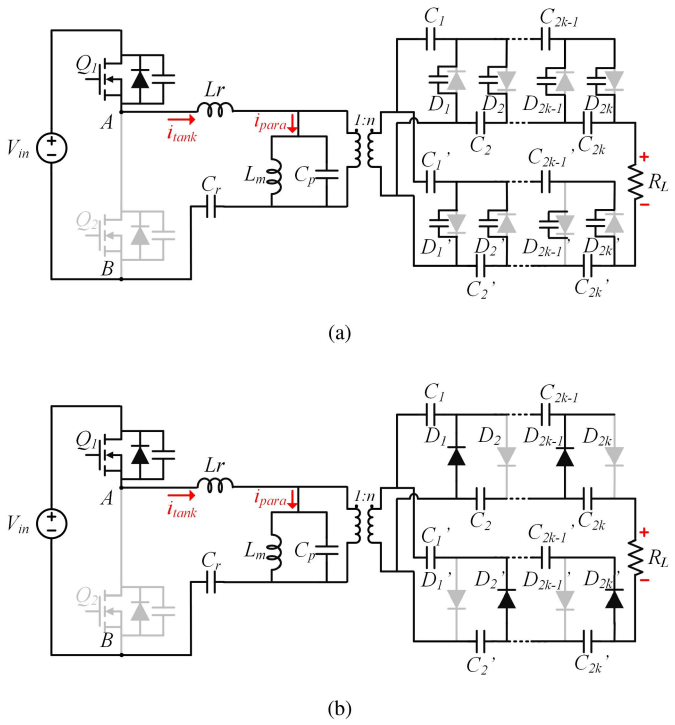

Fig. 4. Device conduction states of the PRC-$LCLC$ resonant converter under different operation modes. (a) Mode 1. (b) Mode 2.

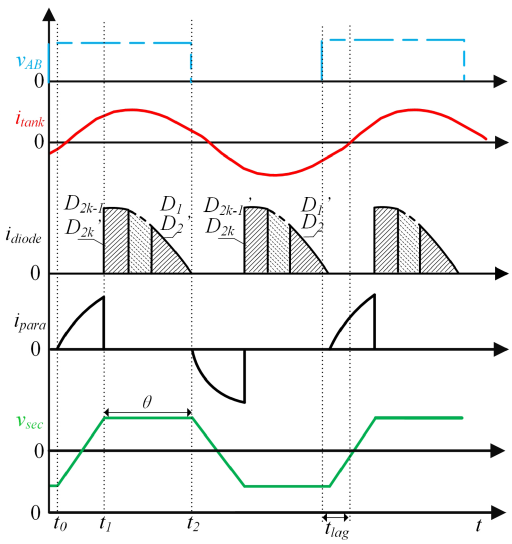

Fig. 5. Typical waveforms of PRC-$LCLC$ resonant converter with the CW voltage multiplier.

The typical waveforms of the PRC-$LCLC$ resonant converter with the dual-polarity CW voltage multiplier are shown in Fig. 5, where v_{AB} is the output voltage of the half-bridge inverter, i_{tank} is the current of the PRC-$LCLC$ resonant tank, i_{para} is the total current flowing through the parallel branch, i_{diode} lumps the current of all diodes, and v_{sec} is the second-side voltage of the step-up transformer.

During the no-conduction mode, the parallel branch is free to participate in the resonance. During the no-conduction mode,

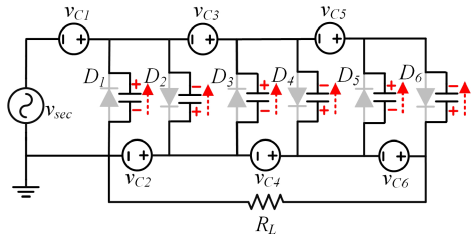

Fig. 6. Direction of displacement current for CW voltage multiplier.

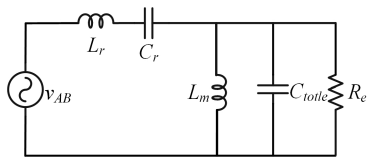

Fig. 7. RCFMA-based model of PRC-$LCLC$ resonant converter.

due to the variation of v_{diode}, all diodes are treated as the no-linear capacitor. Therefore, the accurate estimation of C_j is essential for the steady-state analysis of a CW-voltage-multiplier-based PRC-$LCLC$ resonant converter.

Taking a three-stage up-side CW voltage multiplier as an example, v_{diode} of D_{2k-1} begins to decrease and v_{dioade} of D_{2k} increases during mode 1, thus, the junction capacitance C_j of D_{2k-1} is discharging and the junction capacitance C_j of D_{2k} is charging. The displacement current direction of all diodes is the same for a three-stage single-polarity CW voltage multiplier as shown in Fig. 6, where the capacitors $C_1 \sim C_6$ are treated as voltage sources. Assuming that the output voltage of the per stage CW voltage multiplier is the same, the charge-equivalent C_j during the no-conduction mode can be derived as follows:

$$C_j = \frac{\int_0^{V_R} C_j(v)dv}{V_R} \tag{1}$$

where the reverse voltage of the diode is denoted as V_R. Moreover, the displacement currents of both the up-side and down-side CW voltage multipliers are in the same direction. In this case, the total equivalent capacitance of a k-stage dual-polarity CW voltage multiplier is 4 k C_j.

B. RCFMA-Based Model of PRC-LCLC Resonant Converter

A RCFMA-based model, as depicted in Fig. 7, is introduced for the PRC-$LCLC$ resonant converter with the CW voltage multiplier. The values of the model elements L_r, C_r and L_m, remain consistent with the PRC-$LCLC$ tank. The introduced RC network is comprised of R_e and C_{totle}, where R_e represents the equivalent resistance, C_{totle} includes the equivalent capacitance C_{eq} and the parallel capacitance C_p. C_{eq} acts as an additional compensation capacitor for the resonant converter fed by the behavior of the CW voltage multiplier and load. The coefficient k_c quantifies the relationship between C_{eq} and C_p. In addition, θ corresponds to the conduction angle of the CW voltage multiplier, while a_{v1} and b_{v1} are the Fourier coefficients. The specified derivations are similar to [31], which is skipped

for brevity. The related expressions are provided as follows:

$$R_e = \frac{k_v^2 R_L}{32(nk)^2} \tag{2}$$

$$C_p = n^2(4kC_j + C_w) \tag{3}$$

$$C_{eq} = k_c C_p \tag{4}$$

$$k_c = \frac{2}{k_v(1+\cos(\theta))} \left(\frac{-a_{v1}}{k_v} - \frac{1}{\pi}\sqrt{\left(\frac{1}{2} - \frac{\cos(2\theta)}{2}\right)^2 + \left(\pi - \theta + \frac{\sin(2\theta)}{2}\right)^2} \right) \tag{5}$$

$$C_{totle} = C_p + C_{eq} \tag{6}$$

$$\theta = 2\arctan\sqrt{\frac{4n^2k^2}{f_s C_p R_L}} \tag{7}$$

$$a_{v1} = \frac{2}{\pi}\left(\frac{\sin(\theta) - \pi + \theta}{1+\cos(\theta)} - \sin(\theta)\right) \tag{8}$$

$$b_{v1} = \frac{2}{\pi}(1 - \cos(\theta)) \tag{9}$$

$$k_v = \sqrt{a_{v1}^2 + b_{v1}^2}. \tag{10}$$

The dc voltage gain M of the PRC-$LCLC$ resonant tank at the resonant frequency is given by the following:

$$M = \frac{V_o}{n4kV_{in}} = \frac{2G}{\pi k_v}\sqrt{\eta} \tag{11}$$

where η is the efficiency of the PRC-$LCLC$ resonant converter.

C. Normalized Analysis of PRC-LCLC Resonant Tank

To simplify the investigation of the characteristics of the PRC-$LCLC$ resonant converter, the following definitions are provided:

$$f_{\text{ser}} = \frac{1}{2\pi\sqrt{L_r C_r}} \tag{12}$$

$$f_{\text{par}} = \frac{1}{2\pi\sqrt{L_m C_{\text{totle}}}} \tag{13}$$

$$f_n = \frac{f_s}{f_{paar}} \tag{14}$$

$$Q = \sqrt{\frac{L_m}{C_{\text{totle}}}}\frac{1}{R_e} \tag{15}$$

$$L_n = \frac{L_m}{L_r} \tag{16}$$

$$C_n = \frac{C_r}{C_{\text{totle}}} \tag{17}$$

$$Z_o = \sqrt{\frac{L_m}{C_{totle}}}. \tag{18}$$

Here, f_{ser} and f_{par} are resonant frequencies of the series and parallel branches of the proposed RCFMA model, respectively,

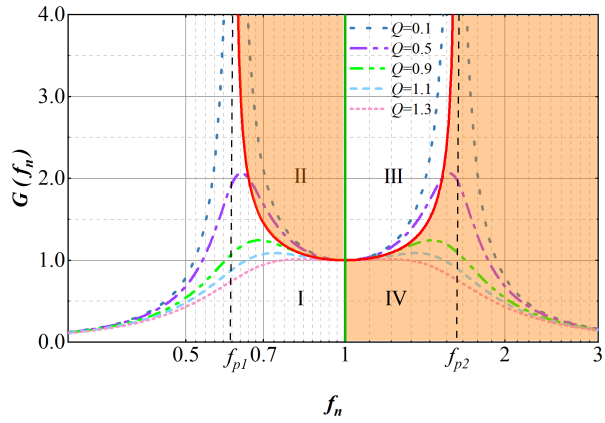

Fig. 8. Magnitude plot of voltage gain under the condition of different Q with $L_n = C_n = 1$ for RCFMA model.

f_n is the normalized frequency, Q is the quality factor, L_n is the normalized inductance ratio, C_n is the normalized capacitance ratio, and Z_o is the characteristic impedance of the PRC-$LCLC$ resonant tank.

The voltage gain and characteristic input impedance of the PRC-$LCLC$ resonant tank are expressed in (19) and (20), respectively. Fig. 8 illustrates the magnitude plot of G for varied Q values, with $L_n = C_n = 1$

$$G = \left| \frac{1}{\left(1 + \frac{1}{C_n} + \frac{1}{L_n}\right) - \left(\frac{1}{C_n f_n^2} + \frac{f_n^2}{L_n}\right) + jQ\left(\frac{f_n}{L_n} - \frac{1}{f_n C_n}\right)} \right| \tag{19}$$

$$\frac{Z_{in}}{Z_o} = \frac{f_n^2 Q}{(1-f_n^2)^2 + f_n^2 Q^2} + j\left[\frac{f_n}{L_n} - \frac{1}{f_n C_n} + \frac{f_n(1-f_n^2)}{(1-f_n^2)^2 + f_n^2 Q^2}\right]. \tag{20}$$

For $Q = 0$, the two resonant frequencies, f_{p1} and f_{p2} correspond to the gain peak of the PRC-$LCLC$ resonant converter, defined as follows:

$$f_{p1} = \sqrt{\frac{A - \sqrt{(A)^2 - 4L_n C_n}}{2C_n}} \cdot f_{\text{par}} \tag{21}$$

$$f_{p2} = \sqrt{\frac{A + \sqrt{(A)^2 - 4L_n C_n}}{2C_n}} \cdot f_{\text{par}} \tag{22}$$

where A is defined as follows:

$$A = C_n + L_n + L_n C_n. \tag{23}$$

Due to the multielement resonance, the component stress can be significantly high, necessitating an analysis of voltage and current stress. Using Kirchhoff's voltage law (KVL), the ac voltage amplitude of the resonant capacitor V_{Cr} and current amplitude of the resonant tank I_{tank} can be calculated as follows:

$$V_{\text{cr}} = \frac{2V_{\text{in}}}{\pi Z_{\text{in}}}\frac{Z_o}{f_n C_n}\sqrt{\eta} + \frac{V_{\text{in}}}{2} \tag{24}$$

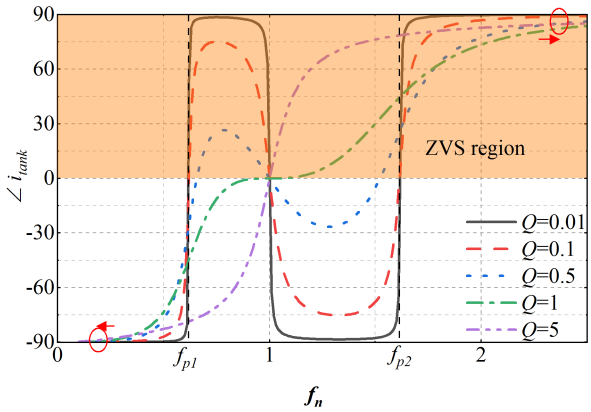

Fig. 9. Plot of lagging angle under condition of different Q with $L_n = C_n = 1$ for RCFMA model.

$$I_{\text{tank}} = \frac{2V_{\text{in}}}{\pi Z_{\text{in}}}\sqrt{\eta}. \tag{25}$$

The lagging angle of i_{tank} with respect to the half-bridge output voltage V_{AB} is essential to realizing ZVS. The lagging angle $\angle i_{\text{tank}}$ is given by the following:

$$\angle i_{\text{tank}} = \frac{180}{\pi}\arctan\left(\frac{\frac{f_n}{L_n} - \frac{1}{f_n C_n} + \frac{f_n(1-f_n^2)}{(1-f_n^2)^2 + f_n^2 Q^2}}{\frac{f_n^2 Q}{(1-f_n^2)^2 + f_n^2 Q^2}}\right). \tag{26}$$

The plot of the lagging angle $\angle i_{\text{tank}}$ is depicted in Fig. 9 with $L_n = C_n = 1$. $\angle i_{\text{tank}} = 0$ marks the boundary between the inductive and capacitive regions for the PRC-$LCLC$ resonant converter, where the ZVS condition can only be achieved in the inductive region.

The purely resistive condition of Z_{in} represents the boundary of the inductive and capacitive regions, simplified as follows:

$$Q^2(f_n) = \frac{f_n}{1-f_n^2}\left(\frac{1}{L_n f_n} - \frac{f_n}{C_n}\right) - \left(\frac{1}{L_n f_n} - \frac{f_n}{C_n}\right)^2 \quad (f_n \neq 1). \tag{27}$$

When $L_n = C_n = 1$, $Q(f_n) = \sqrt{1-(f_n - 1/f_n)^2}$ is derived. Substituting it into (19), the red line of Fig. 8 is achieved. In addition, $f_n = 1$ is another solution of $\text{Im}(Z_{\text{in}}(f_n)/Z_o) = 0$, which is shown as the green line. As depicted in Fig. 8, the red and green lines divide the G-f_n region into four parts: zone I $\sim$ IV. The phase of i_{tank} in zones II and IV lags behind V_A, allowing the PRC-$LCLC$ resonant converter to achieve the ZVS condition. Compared to region I, a wider load range with the ZVS condition as well as a higher switching frequency can be achieved in region IV. In this case, the proposed design methodology is conducted in region IV ($f_n \geq 1$).

III. Design Procedure Based on the Proposed Normalized Analysis

In this section, a voltage-oriented method shown in Fig. 11 is proposed to achieve the required voltage gain of the PRC-$LCLC$ resonant tank with the high efficiency, low component stress, and specific T–R set. The design discussed here mainly focuses on the PRC-$LCLC$ resonant tank, while components such as the output capacitor and the switching devices are not considered.

Four independent parameters needed to be determined: the load condition Q and three normalized parameters f_n, L_n, and C_n. Organizing these four parameters to achieve the desired specifications is the key aspect of designing the PRC-$LCLC$ resonant tank.

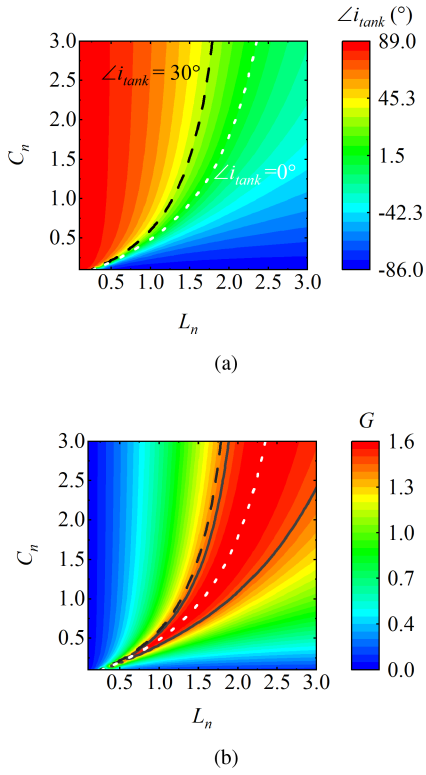

Fig. 10. Contour plot of PRC-$LCLC$ resonant converter with $Q = 0.90$ and $f_n = 1.74$. (a) The lagging angle. (b) G.

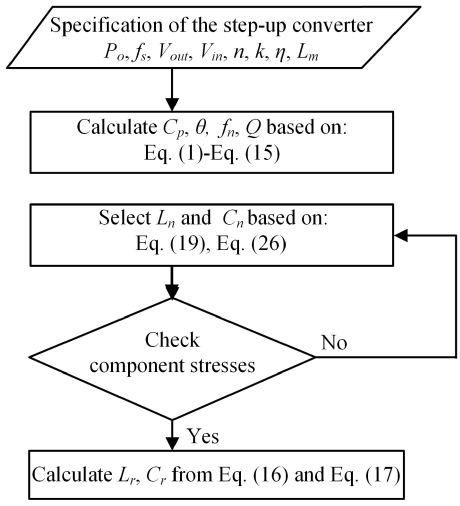

Fig. 11. Design flow chart of PRC-$LCLC$ resonant converter.

TABLE II
SPECIFICATIONS OF PRC-$LCLC$ RESONANT CONVERTER

Parameter	Symbol	Value
Input voltage	V_{in}	25 V
Output voltage	V_{out}	1 kV
Switching frequency	f_s	0.9 $\sim$ 1.5 MHz
Rated Output power	P_o	25 W
Stage of CW voltage multiplier	k	2
Turn ratio of transformer	n	10

A new normalized analysis based on the resonant frequency of the parallel branches is proposed, making the parasitic parameters-composed parallel branches are separated with the PRC-$LCLC$ resonant tank characteristics design. This method allows to adjust L_r and C_r of the series branch to achieve the design resonant tank characteristics, offering a more practical and flexible design process compared to the traditional design methodology.

In the design, the following specifications are given as inputs.

1) Input voltage V_{in}, output voltage V_{out}, output power P_o, and switching frequency f_s.
2) The parameters of the T–R set include the turn ratio n, the magnetic inductance L_m, and the stage of the CW voltage multiplier k.

To further illustrate the selection of the parameters L_n and C_n, take the plots of gain G and phase angle $\angle i_{\text{tank}}$ with specific $Q = 0.90$ and $f_n = 1.74$ as an example, shown in Fig. 10(a) and 10(b), respectively. In Fig. 10(a), the black dash line and white dotted line are $\angle i_{\text{tank}} = 30°$ and $\angle i_{\text{tank}} = 0°$, respectively. In addition, the white dotted line is closed to the gain peak of the PRC-$LCLC$ resonant tank, as shown in Fig. 10(b), where the black line stands for the contour line of $G(L_n, C_n) = 1.5$. For contrast, the black dotted line of $\angle i_{\text{tank}}(L_n, C_n) = 30°$ is also shown in Fig. 10(b).

An ideal selection region of L_n and C_n is formed in the crossed region of $G(L_n, C_n) > 1.5$ and $0° < \angle i_{\text{tank}}(L_n, C_n) < 30°$, in which PRC-$LCLC$ resonant tank can achieve the step-up voltage gain as well as the low lagging angle. In this region, with the increasing of the C_n, the gain ridge becomes wider and the downward gradient of the lag angle is decreasing, indicating the lower component sensitivity. In addition, a minor reduction in C_n or increase of L_n results in a slight increase of G and a decrease of $\angle i_{\text{tank}}$.

IV. EXPERIMENTAL RESULTS

A. Specification of the Step-up Converter

To validate the analysis and design method, a 1-kV, 25-W, MHz-frequency PRC-$LCLC$ resonant converter is designed and built. The converter incorporates a 1:10 turn ratio planar transformer and a 2-stage dual polarity CW voltage multiplier. Specifications for the step-up PRC-$LCLC$ resonant converter are provided in Table II.

The planar transformer uses a Ni-Zn B65513 core from TDK and its winding is implemented on a 6-layer print circuit board (PCB) measuring 11.4 mm $\times$ 21.7 mm. The planar transformer design and the interleaved structure are illustrated in Fig. 12(a) and 12(b), respectively. Specifications of the planar transformer are summarized in Table III. The primary-side equivalent inductance L_k includes both the primary and second leakage inductance of the planar transformer, along with L_m are measured at 1 MHz using the LCR meter. Moreover, C_w is calculated by the resonant frequency between L_m and C_w, as measured with the Impedance analyzer, as shown in Fig. 13.

The PRC-$LCLC$ resonant converter is shown in Fig. 14. This prototype comprises three separate boards (inverter, resonant tank, and rectifier) with the connection by jumpers, which facilitate the current measurement using the TCP0030 probe. The control signals are generated by a TI28335 digital signal processor. In the inverter stage, the GaN high electron mobility

(a) (b)

Fig. 12. Planar transformer: (a) PCB and (b) cross section of winding structure, where Px and Sx represent the primary windings and secondary windings, respectively.

TABLE III
SPECIFICATIONS OF PLANAR TRANSFORMER

Parameter	Symbol	Value
Primary turn number	n_p	4
Secondary turn number	n_s	40
Turn ratio	$1:n$	1:10
Magnetic Inductance	L_m	3.20 μH
Leakage inductance	L_k	0.22 μH
Self resonant frequency	SRF	2.75 MHz
Secondary winding capacitance	C_w	10.50 pF

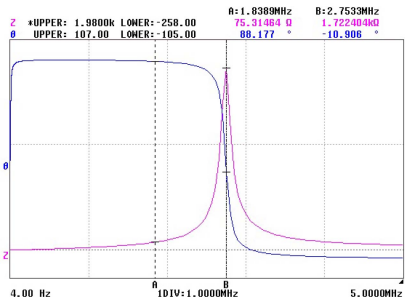

Fig. 13. Measured impedance and phase curves of the planar transformer at the primary side.

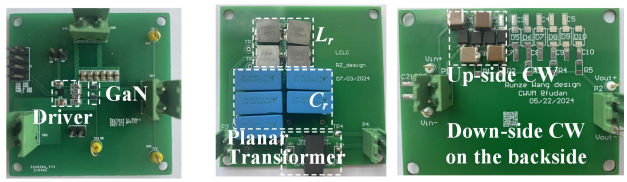

(a) (b) (c)

Fig. 14. Prototype of PRC-$LCLC$ resonant converter. (a) Half-bridge inverter. (b) Resonant components and planar transformer. (c) Dual-polarity CW voltage multiplier.

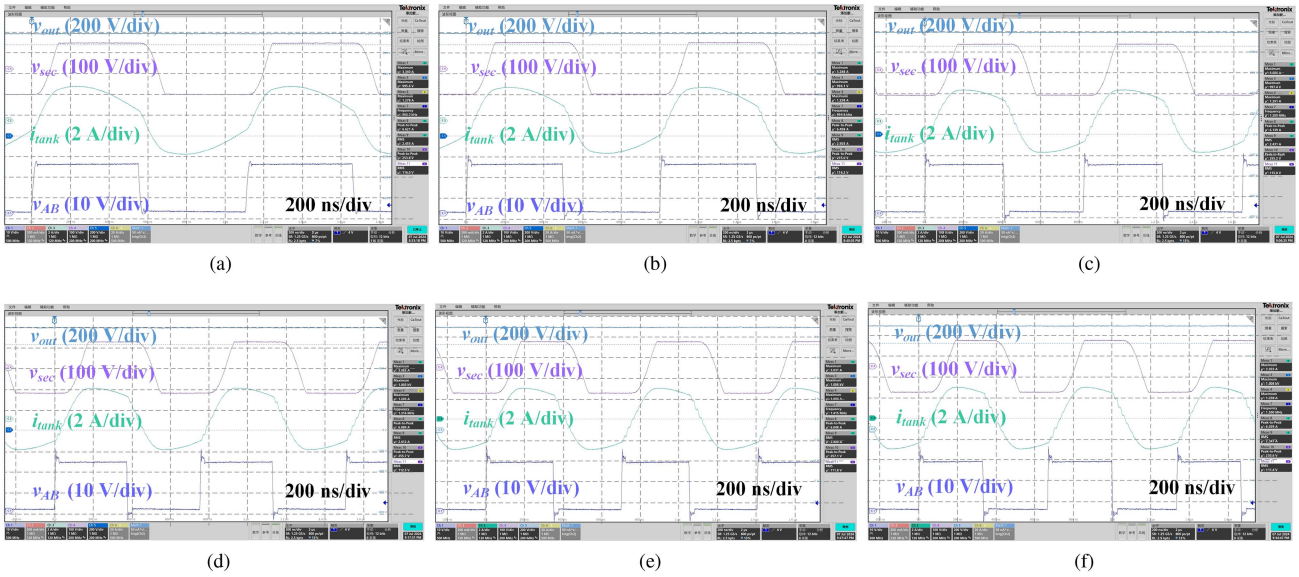

Fig. 15. Experimental waveforms of PRC-$LCLC$ resonant converter at $V_{\text{out}} = 1$ kV with varied f_s and P_o. (a) $f_s = 900$ kHz and $P_o = 24.8$ W. (b) $f_s = 1.0$ MHz and $P_o = 24.1$ W. (c) $f_s = 1.2$ MHz and $P_o = 21.4$ W. (d) $f_s = 1.3$ MHz and $P_o = 20.2$ W. (e) $f_s = 1.4$ MHz and $P_o = 18.6$ W. (f) $f_s = 1.5$ MHz and $P_o = 17.7$ W.

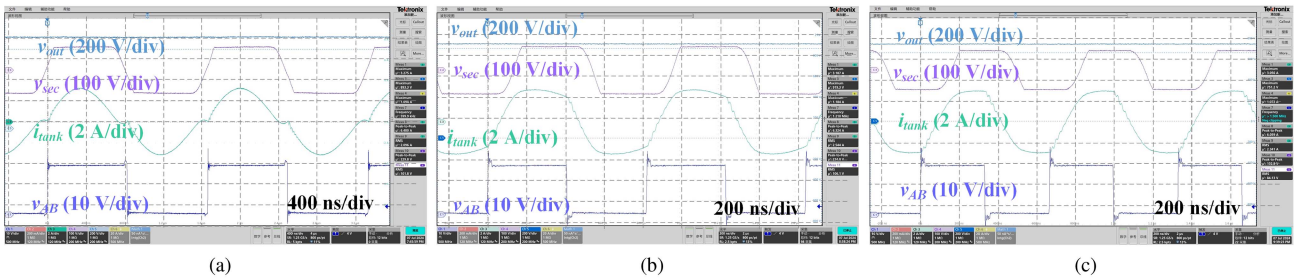

Fig. 16. Experimental waveforms of PRC-$LCLC$ resonant converter at $R_L = 40$ kΩ with varied f_s. (a) $f_s = 600$ kHz. (b) $f_s = 1.2$ MHz. (c) $f_s = 1.5$ MHz.

transistor (HEMT) EPC2014C (40V/ 10A) from EPC is employed.

B. Resonant Tank Design

SiC Schottky diodes effectively address the reverse recovery issues in high-frequency applications. The SiC Schottky diode GB01SLT12-214 (1.2 kV/ 1A) from GeneSiC and two 2-kV/33-nF surface-mount ceramic capacitors (X7R) connected in parallel are applied in the CW voltage multiplier. According to the datasheet and (1), C_j is calculated as 12.8 pF with $V_R = V_{\text{out}}/2\text{ k} = 250$ V.

Based on (2)–(15), C_p, C_{totle}, R_e, f_n, Q, k_v are calculated as 11.29 nF, 25.85 nF, 4.82 Ω, 1.63, 2.31, 1.24, respectively, for $f_s = 900$ kHz, $V_{\text{out}} = 1000$ V and $P_o = 25$ W. Assuming $\eta = 0.85$, the required $G = 1.058$ is derived by (11). In this case, the $\angle i_{\text{tank}}$ and G with respect to L_n - C_n can be plotted as the Fig. 17, where the red region represents the lagging angle from $5^\circ \sim 30^\circ$ and the green region is the gain ridge with $G \geq 1.058$. It is shown that the brown crossed region is formed to achieve the lagging angle as well as the required G for the PRC-$LCLC$ resonant converter.

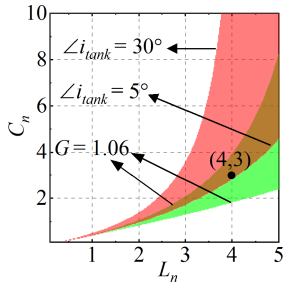

Fig. 17. Curve of recommended lagging angle and required G regions with respect of L_n-C_n.

To reduce the reactive power of the PRC-$LCLC$ resonant tank, $(L_n, C_n) = (4, 3)$ is selected, which is located at the low limit of the lagging angle as depicted in Fig. 17. The resonant inductance L_r is implemented by L_k as well as four surface mounting device inductors connected in parallel from VISHAY

TABLE IV
COMPARISON BETWEEN EXPERIMENT AND THE RCFMA MODEL

f_s/kHz	R_L/kΩ	V_{out}/V			I_{tank}/A			t_θ/ns		
		Exp.	Model	Error	Exp.	Model	Error	Exp.	Model	Error
900	40.0	995	996	0.01%	3.34	3.50	4.8%	418.0	390.8	6.5%
1000	41.2	996	1006	0.9%	3.23	3.58	10.9%	368.2	342.9	6.9%
1100	43.3	998	1009	1.1%	3.16	3.51	10.9%	312.1	302.8	3.0%
1200	46.5	997	1015	1.8%	3.07	3.42	11.4%	277.8	268.3	3.4%
1300	50.0	1002	1017	1.1%	3.05	3.33	9.1%	240.1	239.1	4.0%
1400	54.0	1002	1018	1.6%	3.02	3.25	7.6%	209.2	214.0	2.3%
1500	57.0	1001	993	1.1%	3.00	3.15	4.8%	189.7	193.4	2.0%

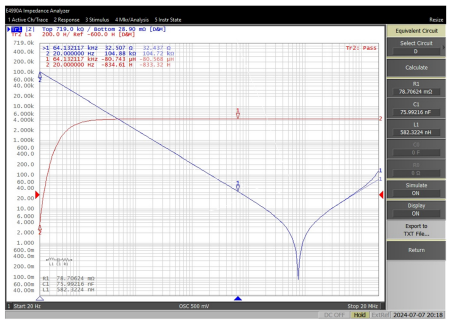

Fig. 18. Measurement of series branch parameters by Impedance analyzer.

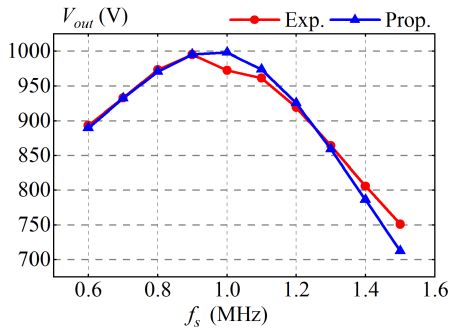

Fig. 19. Frequency response of the output voltage by the experiments and proposed model.

(IHLP-4040, 22A): three inductors of 2.2 μH each and one with 1.5 μH. The resonant capacitance C_r is composed of five 15 nF film capacitors connected in parallel from TDK (B32672L, 700 V). After soldering the components onto the PCB, the values of resonant inductance and capacitance are measured by the Impedance analyzer E4990A from Keysight, as shown in Fig. 18. Together with L_k, the total L_r and C_r are 0.80 μH and 76.0 nF, respectively. The calculated component pressures are $I_{\text{tank}} = 3.5$ A and $V_{Cr} = 20.8$ V within the acceptable limits of the resonant components.

C. Experimental Results

Table IV compares the experimental results with those obtained from the proposed model for the rated V_{out} with varied f_s and load conditions. The parameter t_θ represents the time interval of the corresponded conduction angle θ. The comparison indicates a close agreement between the proposed model and the experiments. The proposed model slightly overestimates I_{tank} because it ignores higher-order harmonics in i_{tank}, resulting in a trapezoidal waveform with reduced amplitude [32]. However, the overestimate is acceptable and does not significantly impact the accuracy of the current pressure estimation.

The waveforms corresponding to Table IV are illustrated in Fig. 15. The ZVS condition is achieved under different conditions. For the light-load condition, the switching frequency is increased to 1.5 MHz to maintain the rated output voltage.

Fig. 19 presents the frequency response of the output voltage by the experiment and the proposed model with $R_L = 40\,\text{k}\Omega$. The partial experimental waveforms are shown in Fig. 16. The ZVS condition is lost at $f_s = 600$ kHz when $\angle i_{\text{tank}} < 0°$, as shown in Fig. 16(a). The model aligns well with the prototype at f_s

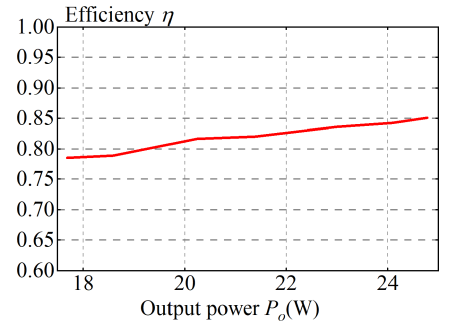

Fig. 20. Measured efficiency of the PRC-$LCLC$ resonant converter.

≤ 900 kHz, increased discrepancies occur when f_s approaches higher frequencies.

The discrepancies can be attributed to the following factors.

1) *Efficiency deviation:* The designed efficiency $\eta = 0.85$ is not maintained under light-load conditions or when the switching frequency is closed to the resonant frequency. Fig. 20 shows that when the output power is around 25 W, the efficiency is around 0.85, and the analytical model gives results with acceptable error. However, as the output power decreases, efficiency, and model accuracy also decline.
2) *Variation of harmonic components:* Fig. 21 further shows the comparison of harmonics (1st–7st) of i_{tank} under three different f_s with $R_L = 40\text{k}\Omega$. It can be found that high-order components decay rapidly, especially when $f_s = 1500$ kHz. However, this variation in harmonic components under different conditions also affects the accuracy of the model.

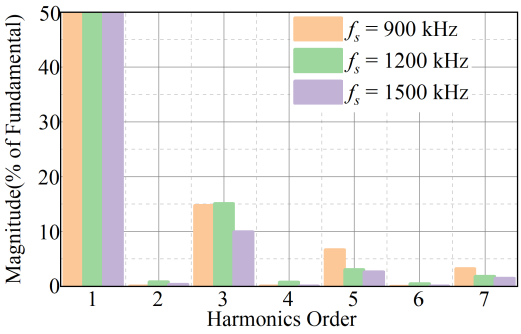

Fig. 21. Comparison of harmonics (1st–7st) of i_{tank} under different f_s with $R_L = 40$ kΩ.

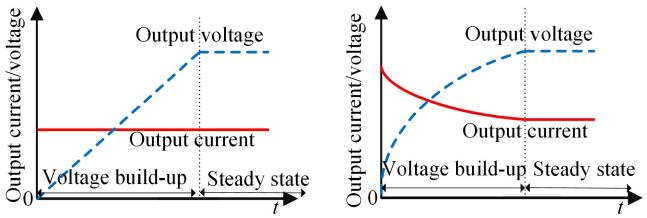

Fig. 22. Two common charging methods. (a) Constant current method. (b) Constant power method.

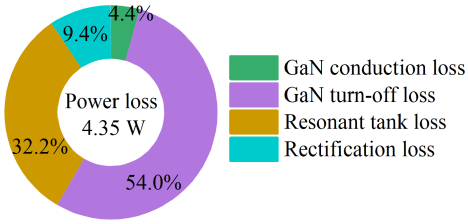

Fig. 23. Power loss breakdown of PRC-$LCLC$ resonant converter at 25 W output.

V. Discussion

A. Controller Design

The control of the high-voltage generator applications is divided into two main phases: the voltage build-up phase and the steady-state operation phase. Two common charging methods, constant current, and constant power charging methods, are shown in Fig. 22(a) and 22(b), respectively.

For the voltage build-up phase, to obey the specified charging method, the f_s to be updated can be deduced by considering the established RCFMA-based model, the amplitude limit of i_{tank} as well as the ZVS condition constraint. During the steady-state control phase, the PI controller can be used. A more detailed controller design can be found in [25].

B. Power Loss Analysis

The power loss breakdown of the PRC-$LCLC$ resonant converter at 25 W is shown in Fig. 23. The resonant tank losses include contributions from the resonant capacitor, resonant inductor, and transformer. The loss analysis reveals that the primary source of losses is the turn-OFF loss (P_{off}). According to (28), P_{off} is related with f_s and the turn-OFF energy E_{off}. It is observed that the percentage of turn-OFF loss is large for PRCs with extremely high f_s (see [33, Fig. 19]). Furthermore, E_{off} increases with the increase of the step-up voltage gain of the resonant tank, which leads to a decrease in efficiency with increased voltage gain of the resonant tank (see [34, Fig. 22]). In fact, achieving the step-up voltage gain of the resonant tank ($M > 1$) while maintaining low E_{off} is contradicted for PRCs with the ZVS condition. This is because an increased M results in a longer turn-OFF time interval for the power switches, thereby increasing the turn-OFF loss [35]

$$P_{\text{off}} = f_s E_{\text{off}}. \tag{28}$$

C. High Power Density Design of High-Voltage Generator Applications

The power density of the planar transformer is calculated as 33.6 kW/L. Several potential design improvements are identified that can further enhance the power density of high-voltage generator applications: 1) Integrating L_r in the design of the step-up planar transformer. 2) Minimizing the number of C_r to reduce the volume of resonant tank. 3) Vertically aligning the up-side and down-side CW voltage multiplier circuits on top and bottom of the PCB to reduce the volume of the rectifier.

VI. Conclusion

A steady-state model and novel normalized analysis are proposed for the PRC-$LCLC$ resonant converter with the planar transformer and CW-voltage multiplier. The proposed model accounts for the nonlinear C_j of rectifier diodes and compensation effects of rectifier behavior. To separate these complex effects with the PRC-$LCLC$ resonant tank characteristics, the novel normalized analysis is conducted on the basis of the resonant frequency of the parallel branch of the RCFMA model. The analysis provides the derivation of the lagging angle, voltage gain, and component stresses of the PRC-$LCLC$ resonant converter. It also introduces a voltage-oriented design methodology for a miniaturized PRC-$LCLC$ resonant converter operating at extremely high switching frequencies without requiring external parallel capacitors. Experimental results validate the high accuracy of the proposed model and confirm the enhanced high-frequency design feasibility and improved parasitic capacitance integration, demonstrating the effectiveness of the proposed design method for practical applications.

References

[1] H. Peng, J. Chen, Z. Cheng, Y. Kang, J. Wu, and X. Chu, "Accuracy-enhanced miller capacitor modeling and switching performance prediction for efficient SiC design in high-frequency X-ray high-voltage generators," *IEEE J. Emerg. Sel. Topics Power Electron.*, vol. 8, no. 1, pp. 179–194, Mar. 2020.

[2] S. Mao, C. Li, W. Li, J. Popovic, S. Schroder, and J. A. Ferreira, "Unified equivalent steady-state circuit model and comprehensive design of the LCC resonant converter for HV generation architectures," *IEEE Trans. Power Electron.*, vol. 33, no. 9, pp. 7531–7544, Sep. 2018.

[3] T. B. Soeiro, J. Muhlethaler, J. Linner, P. Ranstad, and J. W. Kolar, "Automated design of a high-power high-frequency LCC resonant converter for electrostatic precipitators," *IEEE Trans. Ind. Electron.*, vol. 60, no. 11, pp. 4805–4819, Nov. 2013.
[4] R. Hou et al., "Optimization and design of LCC resonant high voltage wide range power supply for magnetrons," *IEEE J. Emerg. Sel. Topics Power Electron.*, vol. 12, no. 4, pp. 3835–3847, Aug. 2024.
[5] S. Yin et al., "A 1-MHz GaN-based LCLC resonant step-up converter with air-core transformer for satellite electric propulsion application," *IEEE Trans Ind. Electron.*, vol. 69, no. 11, pp. 11035–11045, Nov. 2022.
[6] W. Shen et al., "Sunlight-powered sustained flight of an ultralight micro aerial vehicle," *Nature*, vol. 631, no. 8021, pp. 537–543, 2024.
[7] Z. Zhao et al., "Lightweight design of magnetic integrated transformer for high voltage power supply in electro-aerodynamic propulsion system," *IEEE Trans. Power Electron.*, vol. 38, no. 9, pp. 10501–10515, Sep. 2023.
[8] S. Johnson and R. Erickson, "Steady-state analysis and design of the parallel resonant converter," *IEEE Trans. Power Electron.*, vol. 3, no. 1, pp. 93–104, Jan. 1988.
[9] L. Katzir and D. Shmilovitz, "A matrix-like topology for high-voltage generation," *IEEE Trans Plasma Sci*, vol. 43, no. 10, pp. 3681–3687, Oct. 2015.
[10] L. Muller and J. W. Kimball, "High gain DC-DC converter based on the Cockcroft-Walton multiplier," *IEEE Trans. Power Electron.*, vol. 31, no. 9, pp. 6405–6415, Sep. 2016.
[11] S. Mao, J. Popovic, and J. A. Ferreira, "An investigation into high frequency high voltage planar transformer for high voltage generator applications," in *Proc. Int. Conf. Integr. Power Electron. Syst.*, 2016, pp. 1–6.
[12] Z. Ouyang and M. A. E. Andersen, "Overview of planar magnetic technology-fundamental properties," *IEEE Trans. Power Electron.*, vol. 29, no. 9, pp. 4888–4900, Sep. 2014.
[13] Z. Ouyang, O. C. Thomsen, and M. A. E. Andersen, "Optimal design and tradeoff analysis of planar transformer in high-power DC-DC converters," *IEEE Trans. Ind. Electron.*, vol. 59, no. 7, pp. 2800–2810, Jul. 2012.
[14] B. Zhao, G. Wang, and W. G. Hurley, "Analysis and performance of LCLC resonant converters for high-voltage high-frequency applications," *IEEE J. Emerg. Sel. Topics Power Electron.*, vol. 5, no. 3, pp. 1272–1286, Sep. 2017.
[15] S. Zhou, Q. Chen, B. Zhang, J. Gao, C. K. Tse, and L. Xu, "Effects of nonlinear junction capacitance of rectifiers on performance of high voltage power supplies," *IEEE Trans. Power Electron.*, vol. 38, no. 12, pp. 15693–15706, Dec. 2023.
[16] H. Chen and X. Wu, "Analysis on the influence of the secondary parasitic capacitance to ZVS transient in LLC resonant converter," in *Proc. IEEE Energy Convers. Congr. Expo.*, 2014, pp. 4755–4760.
[17] B.-H. Lee, M.-Y. Kim, C.-E. Kim, K.-B. Park, and G.-W. Moon, "Analysis of LLC resonant converter considering effects of parasitic components," in *Proc. IEEE Int. Telecommun. Energy Conf.*, 2009, pp. 1–6.
[18] H. Wen, J. Gong, X. Zhao, C. Yeh, and J. Lai, "Analysis of diode reverse recovery effect on ZVS condition for GaN-based LLC resonant converter," *IEEE Trans. Power Electron.*, vol. 34, no. 12, pp. 11952–11963, Dec. 2019.
[19] N. Shafiei, M. Pahlevaninezhad, H. Farzanehfard, and S. R. Motahari, "Analysis and implementation of a fixed-frequency LCLC resonant converter with capacitive output filter," *IEEE Trans. Ind. Electron.*, vol. 58, no. 10, pp. 4773–4782, Oct. 2011.
[20] Y. A. Ang, C. M. Bingham, M. P. Foster, D. A. Stone, and D. Howe, "Design oriented analysis of fourth-order LCLC converters with capacitive output filter," *IEE Proc. - Electric Power Appl.*, vol. 152, no. 2, pp. 310–322, 2005.
[21] M. T. Outeiro, G. Buja, and D. Czarkowski, "Resonant power converters: An overview with multiple elements in the resonant tank network," *IEEE Ind. Electron. Mag.*, vol. 10, no. 2, pp. 21–45, Jun. 2016.
[22] A. K. Rathore and V. R. Vakacharla, "A simple technique for fundamental harmonic approximation analysis in parallel and series-parallel resonant converters," *IEEE Trans. Ind. Electron.*, vol. 67, no. 11, pp. 9963–9968, Nov. 2020.
[23] I. Batarseh and C. Lee, "Steady-state analysis of the parallel resonant converter with LLCC-type commutation network," *IEEE Trans. Power Electron.*, vol. 6, no. 3, pp. 525–538, Jul. 1991.
[24] R. Oruganti and F. C. Lee, "Resonant power processors, Part I—State plane analysis," *IEEE Trans. Ind. Appl.*, vol. IA-21, no. 6, pp. 1453–1460, Nov. 1985.
[25] M. Qin et al., "Adaptive optimization charging strategy for LCC resonant capacitor charging power supply," *IEEE J. Emerg. Sel. Topics Power Electron.*, vol. 11, no. 6, pp. 5675–5689, Dec. 2023.
[26] J. A. Martin-Ramos, J. Diaz, A. M. Pernia, J. M. Lopera, and F. Nuno, "Dynamic and steady-state models for the PRC-LCC resonant topology with a capacitor as output filter," *IEEE Trans. Ind. Electron.*, vol. 54, no. 4, pp. 2262–2275, Aug. 2007.
[27] D. Fu, F. C. Lee, Y. Qiu, and F. Wang, "A novel high-power-density three-level LCC resonant converter with constant-power-factor-control for charging applications," *IEEE Trans. Power Electron.*, vol. 23, no. 5, pp. 2411–2420, Sep. 2008.
[28] W. Gong, L. Pang, Y. Yao, H. Li, X. Li, and Q. Zhang, "A solid-state high-voltage RF oscillator with CLLC-type resonant topology and its parameter optimization," *IEEE Trans. Power Electron.*, vol. 39, no. 10, pp. 13285–13299, Oct. 2024.
[29] Z. Ye, K. Surakitbovorn, C. H. Lin, and J. Rivas-Davila, "Design of a high-voltage low-ripple converter with high-frequency Dickson multipliers," *IEEE Trans. Ind. Electron.*, vol. 72, no. 1, pp. 401–410, Jan. 2025.
[30] A. Sengupta, U. Kundu, and V. John, "Characteristic-based design of an LCC resonant converter with a capacitive filter," *IEEE Trans. Power Electron.*, vol. 39, no. 3, pp. 3365–3376, Mar. 2024.
[31] G. Ivensky, A. Kats, and S. Ben-Yaakov, "An RC load model of parallel and series-parallel resonant DC-DC converters with capacitive output filter," *IEEE Trans. Power Electron.*, vol. 14, no. 3, pp. 515–521, May 1999.
[32] S.-R. Jang, C.-H. Yu, and H.-J. Ryoo, "Trapezoidal approximation of LCC resonant converter and design of a multistage capacitor charger for a solid-state marx modulator," *IEEE Trans. Power Electron.*, vol. 33, no. 5, pp. 3816–3825, May 2018.
[33] S. Li, X. Yu, Y. Yuan, S. Lu, and T. Li, "A novel high-voltage power supply with MHz WPT techniques: Achieving high-efficiency, high-isolation, and high-power-density," *IEEE Trans. Power Electron.*, vol. 38, no. 12, pp. 14794–14805, Dec. 2023.
[34] Y. Xu et al., "Multimode constant power control strategy for LCC resonant capacitor charging power supply based on state plane analysis," *IEEE Trans. Power Electron.*, vol. 36, no. 7, pp. 8399–8412, Jul. 2021.
[35] R. Wang, S. Mao, S. Yin, H. Liu, Q. Tan, and J. Fan, "Analysis and modeling of zero-voltage-switching condition for LCC resonant converter in above-resonance operation mode," *IEEE Trans. Power Electron.*, vol. 39, no. 9, pp. 10950–10961, Sep. 2024.

Runze Wang received the B.S. and M.S. degrees in electrical engineering from the University of Electronic Science and Technology of China, Chengdu, China, in 2018 and 2021, respectively. He is currently working toward the Ph.D. degree in electrical engineering with the Fudan University, Shanghai, China.

His research interests include wide band gap device applications and high-frequency resonant dc/dc converters.

Saijun Mao (Senior Member, IEEE) received the B.S. and M.S. degrees from Nanjing University of Aeronautics and Astronautics, Nanjing, China, in 2003 and 2006, respectively, the Ph.D. degree from Delft University of Technology, Delft, The Netherlands, in 2018, all in electrical engineering.

From 2006 to 2017, he was a Senior Engineer and Project Leader with the GE Global Research Center, Shanghai, China. He was a Professor with Fudan University, China. He is currently with UniSiC Technology (Shanghai) Company Ltd., China. His research interests include wide-bandgap power semiconductor devices-based high frequency power conversion.

Dr. Mao authored or coauthored more than 70 conference and journal papers. He holds more than 100 issued patents and pending patent applications. He was a recipient of one IEEE Best Paper award and also the recipient of more than 15 awards in GE Global Research Center, including annual technology excellence award, annual technology excellence team award and top inventor award. He served as Session Chair in 2020 IEEE Applied Power Electronics Conference. He was Industry Relations Chairs in 2022 IEEE Transportation Electrification Conference and Expo, Asia-Pacific.

Shan Yin (Member, IEEE) received the B.S. degree in microelectronics from the University of Electronic Science and Technology of China (UESTC), Chengdu, China, in 2010, and the Ph.D. degree in electrical engineering from the Nanyang Technological University (NTU), Singapore, in 2016.

From 2013 to 2016, he was a Research Student and then a Research Fellow with the Rolls-Royce@NTU Corporate Lab, NTU, Singapore, which is a research facility of Rolls-Royce. From 2016 to 2021, he was an Associate Professor with the China Academy of Engineering Physics, Chengdu. From 2021 to 2023, he was a System Engineer with the Innoscience (Shenzhen) Semiconductor Company Ltd., Shenzhen, China. He is currently the System Engineer with the Huawei Technologies Company Ltd., Shenzhen, China. His research interests include wide band gap power device applications.gate drivers, high power density converters, power integration and resonant topologies.

Jinshu Lin (Student Member, IEEE) received the B.S. degree from the Guangdong University of Technology, Guangzhou, China, in 2018, and M.S. degree from the University of Electronic Science and Technology of China (UESTC), Chengdu, China, in 2021, both in electrical engineering. She is currently working toward the Ph.D. degree in electrical engineering with the UESTC.

Her research interests include resonant dc/dc converter and magnetics design.

Hongyao Liu received the B.S. and M.S. degrees in electrical engineering from the Beijing Institute of Technology, Beijing, China, in 2012 and 2015, respectively.

From 2015 to 2016, he was an Engineer with the Qingdao Si fang Rolling Stock Research Institute co., ltd., Qingdao, China. From 2016 to 2019, he was with the Delta Power Electronics Research Center, Shanghai, China. He is a System Engineer with the UniSiC Technology Company Ltd., Shanghai, China. His research interests include wide band gap device applications, gate drivers and high-voltage high-frequency resonant dc/dc converters.

Hui Li (Senior Member, IEEE) received the B.S., M.S. degrees in mechanical manufacturing engineering and Ph.D. degree in aerospace manufacturing engineering from the Northwestern Polytechnical University, Xi'an, China, in 1983, 1987, and 1991, respectively.

From January 2009 to June 2009, he worked as a Visiting Scholar with the University of Toronto, Toronto, Canada. He is currently a Professor with the University of Electronic Science and Technology of China, Chengdu, China. He is also a Member of System Simulation Committee of the Chinese Society of Automation, a Member of Chinese Society of Astronautics, and the Director of Chengdu Mechanical Engineering Society. His research interests include space-craft simulation and fault diagnosis, space-launching technology, intelligent mechanical electrical systems, and power electronics.

Jiajie Fan (Senior Member, IEEE) received the Ph.D. degree in industrial and systems engineering from the Hong Kong Polytechnic University, Hung Hom, Hong Kong, in 2014.

He is currently a Youth Researcher with the Academy for Engineering and Technology and Shanghai Engineering Technology Research Center for SiC Power Device, Fudan University, Shanghai, China. His main research interests include prognostics and health management and wide bandgap power electronics packaging and reliability modeling.

Dr. Fan is an Associate Editor of IEEE ACCESS JOURNAL.